





**Zero-field propagation of spin waves in waveguides prepared by focused ion beam direct writing**Lukáš Flajšman <sup>1,\*</sup>, Kai Wagner <sup>2</sup>, Marek Vaňatka,<sup>1</sup> Jonáš Gloss,<sup>3</sup> Viola Křížáková <sup>4</sup>, Michael Schmid,<sup>3</sup> Helmut Schultheiss <sup>2</sup> and Michal Urbánek<sup>1,4,†</sup><sup>1</sup>*CEITEC BUT, Brno University of Technology, 61200 Brno, Czech Republic*<sup>2</sup>*Institute of Ion Beam Physics and Materials Research, HZDR, 01328 Dresden, Germany*<sup>3</sup>*Institute of Applied Physics, TU Wien, 1040 Vienna, Austria*<sup>4</sup>*Institute of Physical Engineering, Brno University of Technology, 61669 Brno, Czech Republic*

(Received 18 July 2019; revised manuscript received 18 September 2019; published 24 January 2020)

Metastable face-centered-cubic Fe<sub>78</sub>Ni<sub>22</sub> thin films are excellent candidates for focused ion beam direct writing of magnonic structures due to their favorable magnetic properties after ion-beam-induced transformation. The focused ion beam transforms the originally nonmagnetic fcc phase into the ferromagnetic bcc phase with additional control over the direction of uniaxial magnetic in-plane anisotropy and saturation magnetization. Local magnetic anisotropy direction control eliminates the need for external magnetic fields, paving the way towards complex magnonic circuits with waveguides pointing in different directions. In the present study, we show that the magnetocrystalline anisotropy in transformed areas is strong enough to stabilize the magnetization in the direction perpendicular to the long axis of narrow waveguides. Therefore, it is possible to propagate spin waves in these waveguides in the favorable Damon-Eshbach geometry without the presence of any external magnetic field. Phase-resolved microfocused Brillouin light scattering yields the dispersion relation of these waveguides in zero as well as in nonzero external magnetic fields.

DOI: [10.1103/PhysRevB.101.014436](https://doi.org/10.1103/PhysRevB.101.014436)**I. INTRODUCTION**

Nowadays, the vibrant field of magnonics stands on the edge between the development of elementary building blocks of magnonic circuitry and envisioned all-magnon on-chip devices [1,2]. The magnonic devices, utilizing the physics of spin waves, are recognized to have potential in information processing in the frequency range from gigahertz to terahertz. High frequencies together with low energy of elementary excitations render the magnonic devices suitable for beyond-CMOS computational technologies. Many concepts of future devices used for steering and manipulating spin waves have been presented recently [3–6]. To allow further advances in this field, new types of materials possessing additional means of control over their magnetic properties together with good spin-wave propagation are needed.

Here we show that magnonic waveguides with fast spin-wave propagation at zero magnetic field can be directly written into metastable Fe<sub>78</sub>Ni<sub>22</sub> thin films by a focused ion beam (FIB). The local dose and scanning strategy control both the saturation magnetization and the magnetocrystalline anisotropy (direction, type, and strength) of irradiated areas. The unique possibilities of this material system allow one to overcome the shape anisotropy of long magnonic waveguides and stabilize the magnetization perpendicular to the direction of the waveguide even in the absence of any external magnetic field. This is of great importance for using magnons as information carriers because the geometry where the

magnetization is aligned perpendicularly to the propagation direction has the maximum group velocity (Damon-Eshbach modes).

The Fe<sub>78</sub>Ni<sub>22</sub> layers grow on a Cu(001) substrate in the metastable nonmagnetic fcc phase and can be transformed by ion irradiation into the ferromagnetic bcc phase [7,8]. Using a FIB, the fcc→bcc transformation can be precisely controlled, which results in unprecedented local control over the magnetic properties [9]. This approach removes the need for complicated multistep lithography processing and provides rapid prototyping of individual structures on the sample with the additional possibility to control the magnetic properties of each structure or even to change the magnetic properties locally in a single magnetic element [9–12]. This approach is more versatile than the conventional approaches, which use external magnetic fields or global magnetic anisotropy for stabilizing and controlling the spin-wave propagation. The highly local character of the presented approach allows stabilizing the magnetization in the direction of the locally variable magnetic anisotropy. Classical approaches of nanostructuring of magnetic materials such as optical or electron beam lithography combined with lift-off processing [13], wet [14] or dry [15] etching, or ion implantation [16,17] do not offer the same control over local material properties. The same is true for fabrication processes that rely on a binary selection of adding or removing the magnetic materials.

**II. EXPERIMENTS**

The FIB-written waveguides together with a microwave antenna for spin-wave excitation are shown in Fig. 1(a). The

\*lukas.flajsman@ceitec.vutbr.cz

†michal.urbanek@ceitec.vutbr.cz

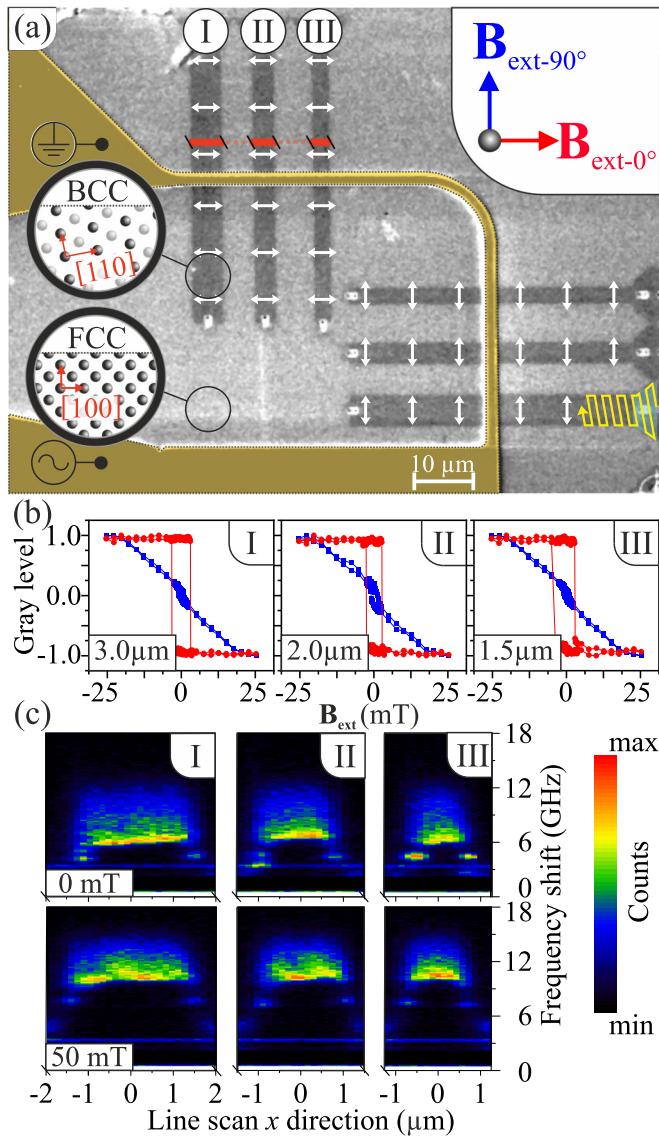


FIG. 1. (a) SEM micrograph of FIB-prepared waveguides (bcc waveguides appear dark gray). The crystallographic orientations of the fcc matrix and bcc waveguides are indicated (for the latter, inferred from the magnetic anisotropy, double-headed arrow). The microwave antenna is highlighted in ocher. The FIB irradiation strategy is schematically shown in the bottom-right structure by the yellow zigzag path. In the same structure, the overlaid cyan pattern highlights the growth initiation triangular region which has been irradiated with an increased ion dose. (b) Hysteresis loops of three waveguides for two different orientations of the magnetic field [blue and red curves correspond to the orientations of the magnetic field indicated by arrows in the top-right corner of (a)]. (c) 2D frequency maps of thermal spin-wave spectra measured by microfocused BLS scanning over the waveguides in the transverse direction along the red lines in zero external magnetic field (top row) and in an applied magnetic field  $B_{\text{ext}-0^\circ} = 50$  mT (bottom row). The spatially and magnetic-field-invariant mode at approximately 3 GHz is a spurious laser mode.

waveguides are 30 μm long with nominal widths of 3, 2, and 1.5 μm and are clearly visible in the SEM image.

Prior to the FIB processing, the metastable fcc Fe<sub>78</sub>Ni<sub>22</sub> thin film of nominal thickness 12 nm was grown under UHV conditions on a Cu(001) single-crystal substrate using the procedure described in Ref. [8]. After deposition, the sample was transferred to the FIB-SEM microscope for FIB irradiation. We oriented the long axis of the waveguides along the fcc[010] direction of the Cu substrate in order to obtain the highest possible magnetocrystalline anisotropy [9]. To imprint the anisotropy direction perpendicularly to the long axis of the waveguide, we wrote the structures with a single pass of a 30 keV Ga<sup>+</sup> ion beam (30 nm spot, beam current of 150 pA, and 5 μs dwell time) with the fast scanning direction rotated by 80° from the waveguide's long axis [see the bottom-right structure in Fig. 1(a)]. The resulting ion dose of  $4 \times 10^{15}$  ions/cm<sup>2</sup> has given reliable growth conditions for all the waveguides. Nucleation of the bcc structure was facilitated by starting the growth in a triangular 5-μm-wide region with the doubled ion dose of  $8 \times 10^{15}$  ions/cm<sup>2</sup> (again in a single FIB scan).

After the irradiation, the magnetic waveguides were investigated with Kerr magnetometry [18] and Kerr microscopy. When the field  $B_{\text{ext}-90^\circ}$  is applied parallel to the long axis of the waveguide, hard-axis hysteresis loops [blue lines in Fig. 1(b)] with effective anisotropy fields [19] in the range 20–25 mT are observed for all waveguides. When the field  $B_{\text{ext}-0^\circ}$  is applied perpendicular to the waveguide, easy-axis loops [red lines in Fig. 1(b)] with coercive fields in the range of 4–8 mT are observed.

Thermal spin-wave spectra obtained by microfocused Brillouin light scattering microscopy [20] are shown in Fig. 1(c) for zero magnetic field and for the external field  $B_{\text{ext}-0^\circ} = 50$  mT. The signal is proportional to the density of spin-wave states at the detection frequency (y axis) and shows pronounced spin-wave spectral intensity localized solely in the areas irradiated by the FIB. The bandgap of the spin-wave band structure for the middle of the waveguide ( $x = 0$  μm) can be clearly seen as a sudden increase in the density of spin-wave states for frequencies higher than approximately 6 GHz in zero field and at approximately 10 GHz in the external field of 50 mT.

All three waveguides show qualitatively the same behavior. The data also reveal the local change in spin-wave spectra towards the sides of the waveguide. Here localized low-frequency modes appear at approximately 4 GHz in zero field and at approximately 8 GHz in the external field of 50 mT. This is a clear indication of the transverse orientation of the magnetization and its inherent demagnetizing field leading to lower effective fields at the waveguide edges and thus directly resulting in the localized spin-wave edge modes [21,22]. The overall analysis is depicted for three vertically oriented waveguides only as the behavior of the horizontally oriented waveguides shows qualitatively the same behavior (the anisotropy is again imprinted perpendicularly to the long axis of the waveguides). This also demonstrates the unique potential of our approach when compared to other less versatile approaches or materials with global magnetocrystalline anisotropy.

In the following experiments, we extract the magnetic field dependence of the spin-wave dispersion relation. By fitting the measured dispersion, we were able to obtain the full set

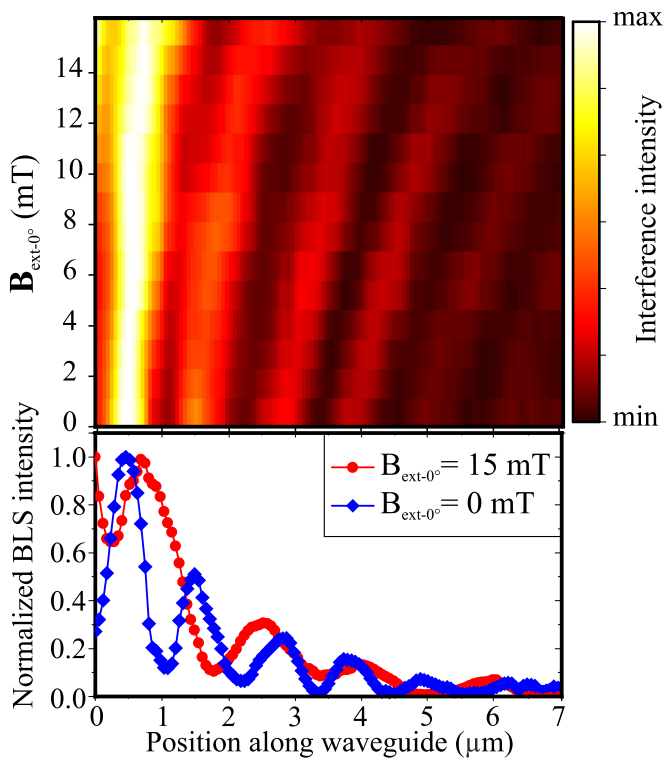


FIG. 2. Phase-resolved BLS microscopy interference intensity map for various external magnetic fields at a fixed excitation frequency of 10.2 GHz. Individual line scans have been normalized and a space-invariant background was subtracted. The bottom graph shows line profiles extracted from the intensity map for 15 mT (red line) and for zero external magnetic field (blue line).

of magneto-dynamic parameters of the material. The standard  $\mu$ BLS method cannot directly sense the phase of the detected spin waves, and thus it does not allow to determine the wavelength  $\lambda$  (or equivalently the wave propagation vector  $\vec{k}$ ) of the spin waves. In order to extract the wave-vector information, we employed the phase-resolved  $\mu$ BLS technique [20,23]. The method directly reveals the spatial profile of the spin-wave phase by letting the scattered photons interfere with a reference signal of a constant phase created by an electro-optic modulator (EOM).

We recorded the interference signal along the 1.5  $\mu\text{m}$  wide waveguide ( $x = 0 \mu\text{m}$ ) with a step size of 120 nm from the edge of the exciting antenna up to 7  $\mu\text{m}$  distance at a microwave frequency of 10.2 GHz. The phase-resolved measurements are shown in Fig. 2.

We measured the BLS interference line scans with an applied external magnetic field (perpendicular to the waveguide long axis) from 0 to 15 mT (1 mT step). The BLS interference intensity map shows a gradual increase of the spin-wave wavelength from the lowest value of 1.09  $\mu\text{m}$  found at zero field up to 1.60  $\mu\text{m}$  at 15 mT. This is additional evidence for the presence of the Damon-Eshbach geometry even at zero field since otherwise a decreasing wavelength with increasing field would be expected. To extract the spin-wave wavelength, we fitted the measured data with the simple interference model:

$$I(y) = I_{\text{SW}}(y) + I_{\text{EOM}} + 2\sqrt{I_{\text{SW}}(y)I_{\text{EOM}}}\cos[\theta(y)], \quad (1)$$

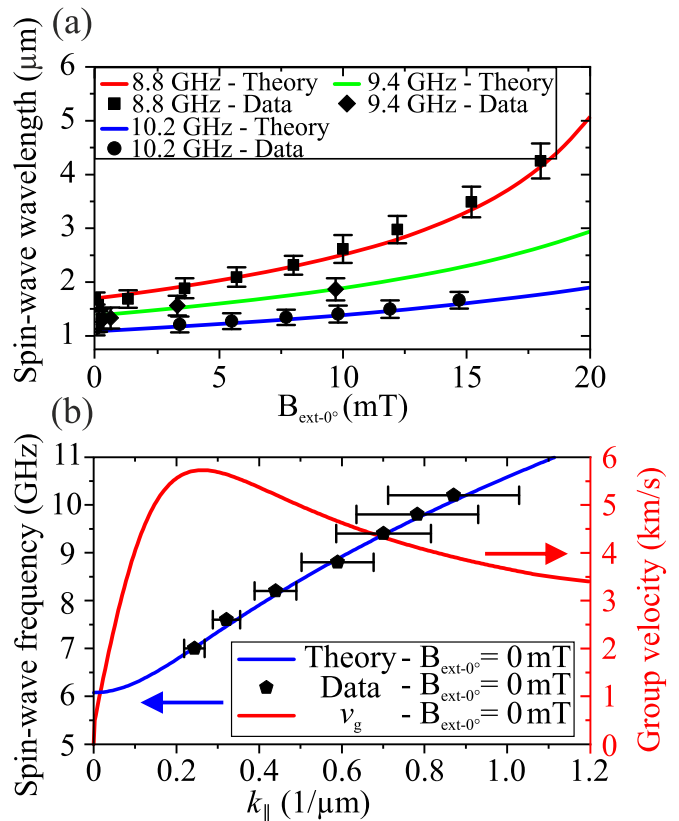


FIG. 3. (a) Dependence of the spin-wave wavelength  $\lambda_l$  [extracted from Eq. (1)] on the external magnetic field for three different frequencies fitted with the model given by Eq. (2). (b) Experimental and calculated (blue line) spin-wave dispersion together with the calculated group velocity (red line) at zero external magnetic field. The error bars have been calculated from the 95% fit confidence bounds.

where we assume  $I_{\text{SW}} = I_{\text{max}}e^{-y/L_{\text{att}}}$ . The parameters  $I_{\text{EOM}}$  and  $I_{\text{max}}$  are EOM and spin-wave maximum intensities,  $L_{\text{att}}$  is a spin-wave attenuation length, and the total phase difference is  $\theta = 2\pi\frac{y}{\lambda_l} + \theta_0$  with  $\lambda_l$  representing the longitudinal spin-wave wavelength,  $y$  is the distance from the excitation antenna, and  $\theta_0$  is an arbitrary phase offset between the EOM and the spin-wave excitation. We fitted the experimental data using Eq. (1) with all five parameters unconstrained. The two important fit parameters are the wavelength [shown in Fig. 3(a) as a function of  $B_{\text{ext}}$ ] and the attenuation length. The largest attenuation length  $L_{\text{att}} = 3.1 \pm 0.4 \mu\text{m}$  is measured for zero external magnetic field and the frequency of 10.2 GHz. The spin-wave dispersion at zero field obtained from these fits is shown in Fig. 3(b).

### III. MODELING AND DISCUSSION

From the dispersion, we can determine the magnetic parameters using the model of Kalinikos and Slavin [24], while taking into account the finite width of our waveguides by assuming the effective boundary conditions as described by Guslienko *et al.* [25]. The effective dipolar conditions yield an effective width  $w_{\text{eff}} = wd/(d-2)$  of the waveguide, determined by the geometric width  $w$  and the pinning

parameter  $d = 2\pi/[p + 2p\ln(1/p)]$ . The parameter  $p$  is given by  $p = t/w$ , where  $t$  is the thickness of the magnetic material. For the spin-wave dispersion model, we assumed that the external magnetic field  $B_{\text{ext}}$  points in the direction of the magnetic anisotropy, i.e., perpendicularly to the long edge of the waveguide (magnetic anisotropy is introduced in the form of an effective magnetic field  $B_{\text{ani}}$ ). With all the terms in place the model is the following:

$$\frac{f^2}{\gamma^2} = [ |B_{\text{ext}}| + |B_{\text{ani}}| + \mu_0 M_s P \sin^2(\angle k) + (2A_{\text{ex}}/M_s) |\vec{k}|^2 ] \times [ |B_{\text{ext}}| + |B_{\text{ani}}| + \mu_0 M_s (1 - P) + (2A_{\text{ex}}/M_s) |\vec{k}|^2 ] \quad (2)$$

where  $f$  is the spin-wave frequency and  $\gamma$  is the gyromagnetic ratio.  $M_s$  is the saturation magnetization and  $A_{\text{ex}}$  is an exchange stiffness.  $\angle k$  is an angle of the spin-wave propagation with respect to the long axis of the waveguide. It is calculated from the respective orthogonal components of the propagation vector as  $\angle k = \text{atan}(k_{\parallel}/k_{\perp n})$ . The longitudinal component of the total propagation vector is  $k_{\parallel}$  (parallel to the long axis of the waveguide) and the transverse (quantized) component is  $k_{\perp n}$ . Since the thickness of the waveguide is small with respect to the other dimensions and the spin-wave wavelength, we only calculate the first branch of spin waves along the thickness  $t$ , yielding  $P = 1 - [1 - \exp(-|\vec{k}|t)]/|\vec{k}|t$ . The total propagation vector is given by  $|\vec{k}| = \sqrt{k_{\parallel}^2 + k_{\perp n}^2}$ . The amplitude of the transverse component  $k_{\perp n}$  is calculated from the width quantization condition  $k_{\perp n} = n\pi/w_{\text{eff}}$  for  $n = 1, 2, \dots$ . In the microfocused BLS experiment, as we record only the interference pattern along the long waveguide axis, we see only the longitudinal component of the propagation vector  $k_{\parallel} = 2\pi/\lambda_1$ .

We performed the fit using Eq. (2) [considering 95% confidence intervals obtained by fitting of Eq. (1)] for various width modes (and their linear combinations [26,27]) with a single set of unconstrained universal parameters, and we minimize the total residuals of the fit. The best fit was found using a single mode ( $n = 1$ ) only (in contrast to experiments in, e.g., permalloy waveguides [26,27]), with magnetic parameters of  $M_s = 1.41 \pm 0.03$  MA/m,  $\gamma = 29.3 \pm 0.1$  GHz/T,  $B_{\text{ani}} = 24 \pm 1$  mT,  $t = 9.5 \pm 1.0$  nm,  $A_{\text{ex}} = 11 \pm 5$  pJ/m, and  $w = 1.62 \pm 0.05$   $\mu\text{m}$  (for the 1.5  $\mu\text{m}$  wide waveguide, II in Fig. 1). The obtained fit parameters lie close to the bulk values of single-crystal iron films [28]. The saturation magnetization  $M_s = 1.41$  MA/m is expectedly lower than the bulk value of iron ( $M_s^{\text{Fe}} = 1.7$  MA/m). If we consider 22% of nickel ( $M_s^{\text{Ni}} = 0.51$  MA/m) in our films and assume a linear dependence on composition, we estimate the expected saturation magnetization to be  $M_s^{\text{FeNi}} = 1.45$  MA/m, which is very close to the value  $M_s = 1.41$  MA/m obtained from the fit. The large saturation magnetization together with the Damon-Eshbach geometry result in a high group velocity  $v_g = \partial f / \partial k_{\parallel}$  of the spin waves reaching almost 6 km/s [see Fig. 3(b)]. The anisotropy field resulting from the fit perfectly reproduces the value measured by Kerr microscopy, which further supports the validity of the model. The fitted thickness is very close to the nominal thickness of 12 nm (the few topmost layers are expected to oxidize when performing

*ex-situ* experiments) which indicates that the film is transformed to the magnetic bcc phase throughout the whole thickness. This is also supported by the Monte Carlo ion stopping range simulations using the SRIM/TRIM package [29], where more than 90% of the 30 keV  $\text{Ga}^+$  ions penetrate to the copper substrate. The width of the waveguide  $w = 1.62$   $\mu\text{m}$  is slightly larger than the nominal value (1.5  $\mu\text{m}$ ). First and presumably the major contribution increasing the width of the waveguide is the finite size and shape of the focused ion beam spot. Furthermore, in our previous work on thinner films [30], it was shown that the bcc crystallites protrude into the fcc phase from the ion impact spot, and thus they also effectively increase the width of the waveguides (the protrusion length was approximately 50 nm). Both effects effectively create a gradient in the magnetization affecting the dynamic boundary conditions of our waveguides [31], which differs from the discontinuous boundary conditions found, e.g., in structures prepared by classical lithography techniques [26,27]. We performed micromagnetic simulations in mumax<sup>3</sup> [32] to study the effects of the magnetization gradient at the waveguide edges on the spin-wave dispersion. For a detailed description of the micromagnetic study see the Appendix. In the simulations we continuously decreased the magnetization from the bulk value to zero in a defined region at the edge of the waveguide (see definition in the Appendix). The introduced profile of the magnetization was chosen as an error function as it resembles the convolution of the nominal shape of the waveguide with a FIB spot. Due to the gradient of the saturation magnetization, it is expected that the local spin-wave dispersion will differ from the discontinuous case where the saturation magnetization changes abruptly [31]. The transverse profiles of the saturation magnetization together with the simulated effective (internal) magnetic field at zero external magnetic field are shown in Fig. 4(a).

The micromagnetic simulations reveal that an infinite gradient in the magnetization leads to a sharp spike of the effective magnetic field ( $B_{\text{eff}}$ ) at the edges of the waveguide. In the case of finite magnetization gradient, the  $B_{\text{eff}}$  profile becomes smeared out. The maximum value of the  $B_{\text{eff}}$  is lower and the central homogeneous region is significantly broadened, as the lower gradient of the magnetization leads to a lower and less localized demagnetizing field. The simulations also showed that for both cases in a narrow region near the edges of the waveguide the magnetization realigns to the longitudinal direction. The longitudinal spin-wave dispersion extracted from the micromagnetic simulations is plotted in Fig. 4(b). There is an obvious difference in the modal structure of the dispersion when we compare the cases with  $\sigma = 0$  nm and  $\sigma = 25$  nm. As the gradient is introduced to the edge region, the boundary conditions for the dynamic magnetization are altered. The quantization of the modes with higher transverse mode numbers is deteriorated. As a direct consequence, the modes with higher transverse  $k$  vector get weaker (as can be seen from a lower power spectral density). The first waveguide mode does not significantly change even for  $\sigma = 100$  nm. This is likely the main mechanism explaining the absence of any higher-order waveguide modes seen in the phase-resolved BLS data (Fig. 2). This statement is further supported by a careful analysis of the line scans. To confirm the visual impression

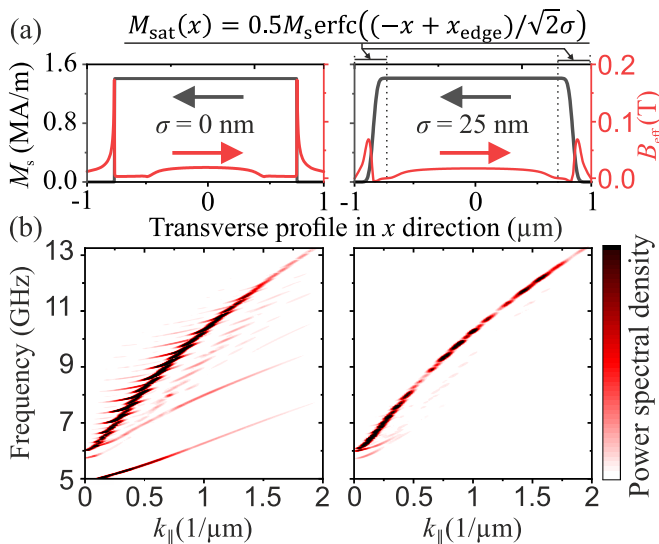


FIG. 4. (a) Transverse profiles of the saturation magnetization (dark gray) and effective magnetic field (red) for a discontinuous (left panel) and continuous (right panel) transition of the saturation magnetization on the edges of the waveguide at zero external magnetic field for the material parameters obtained by the fitting procedure. The continuous transition was implemented as a quasicontinuous modulation of  $M_s$  expressed by the equation shown above the plots. The transition width ( $\sigma$ ) of the complementary error function is designated in each plot. (b) dispersion relations of the spin-wave modes for both magnetization profiles extracted from micromagnetic simulations. The power spectral density of the modes (represented by the color scale) has been normalized to the maximum value.

we have extended Eq. (1) to allow for more overtone spatial frequencies [as expected by Eq. (2)] to be detected since we expect from the modal profiles of the analytical model presented by Eq. (2) to excite multiple odd modes [27,33] at certain frequencies by the excitation antenna. This analysis confirmed the results of the micromagnetic simulation as the best agreement is found in the absence of any higher spatial frequencies.

#### IV. CONCLUSIONS

We have studied the spin-wave propagation in waveguides prepared by FIB direct writing into metastable fcc Fe<sub>78</sub>Ni<sub>22</sub> thin films. We have shown that in these high-aspect-ratio waveguides spin waves can propagate with high group velocities reaching almost 6 km/s without the necessity of external magnetic fields or global magnetic anisotropy. This unique feature is realized by the local uniaxial magnetic anisotropy, which is controlled by the writing procedure [9]. The spin-wave dispersion relation has been determined by using phase-resolved BLS microscopy and the magnetic properties of the waveguides were extracted. The relatively large saturation magnetization together with high (controllable) magnetic anisotropy render the material suitable for high-frequency spin-wave circuits operational even at zero external magnetic field. Moreover, the extracted material properties of the system will allow us to design more complex spin-wave devices by utilizing the possibility to spatially control both the

saturation magnetization and the direction of the uniaxial magnetic anisotropy in a single magnetic structure. Our unique approach paves the way towards many other possibilities to develop and study spin-wave propagation in magnetization landscapes that are unattainable in any conventional magnetic system.

#### ACKNOWLEDGMENTS

This research has been financially supported by the joint project of Grant Agency of the Czech Republic (Project No. 15-34632L) and Austrian Science Fund (Project I 1937-N20) and by the CEITEC Nano+ project (ID CZ.02.1.01/0.0/0.0/16013/0001728). Part of the work was carried out in the CEITEC Nano Research Infrastructure (ID LM2015041, MEYS CR, 2016–2019). L.F. was supported by a Brno Ph.D. talent scholarship.

#### APPENDIX: MICROMAGNETIC MODELING

In order to obtain the spin-wave dispersion of a magnonic waveguide with a continuous magnetic-to-nonmagnetic transition at the waveguide edges, we employed the free GPU-accelerated finite difference solver mumax<sup>3</sup> [32] and the procedure described, e.g., in Ref. [34]. Mumax<sup>3</sup> allows one to define up to 256 regions, in which the material parameters can be individually defined. In our approach, the waveguide “core” has a constant value of the saturation magnetization  $M_s$ , whereas the edge regions have a saturation magnetization that decreases quasicontinuously from the maximum value of  $M_s$  to zero. Figure 5 depicts the geometry definition of the problem.

The saturation magnetization spatial modulation has been chosen in the form of a complementary error function because it resembles the convolution of nominal geometry with the spot of the focused ion beam (approximated by a Gaussian beam profile):  $M_{\text{sat}}(x) = 0.5M_s \text{erfc}[(-x + x_{\text{edge}})/\sqrt{2}\sigma]$ . The inflection point of the error function is denoted  $x_{\text{edge}}$ ; the decay region extends by  $\pm 4\sigma$  to both sides of  $x_{\text{edge}}$ , where  $\sigma$  is the standard deviation of the Gaussian that the error function is based on (we chose  $\sigma = 25$  nm). This ensures a smooth transition to the core region with constant saturation magnetization  $M_{\text{sat}} = M_s$  and the periphery with  $M_{\text{sat}} = 0$ . The distance between the two inflection points is chosen larger than the nominal width  $w_{\text{nominal}}$  by 100 nm ( $4\sigma$ ), to account for the growth of the magnetic bcc structure into the nonirradiated area, as mentioned above. This setup, shown in Fig. 5, results in a total width of the simulation cell of  $W = w_{\text{core}} + 16\sigma = w_{\text{nominal}} + 12\sigma$ . The discretization grid spacing was chosen as  $\Delta x = 3.52$  nm,  $\Delta y = 14.7$  nm, and  $\Delta z = 9.5$  nm. The rather large value of  $\Delta y$  is due to computational reasons as for good resolution in the reciprocal space (small step in  $k_{\parallel}$ ) the simulated geometry needs to be rather large. The resolution of  $k_{\parallel}$  is determined by  $1/(n_y \Delta y)$  where  $n_y$  is the number of elements in the  $y$  direction. The resulting grid size for the data presented in Fig. 4 with  $\sigma = 25$  nm, and  $w_{\text{nominal}} = 1.5$   $\mu\text{m}$  was 2048 points in  $y$  and 512 points in  $x$ . Thus, the simulated geometry was  $30\,000 \times 1800 \times 9.5$  nm<sup>3</sup> large.

The material parameters were chosen to  $M_s = 1.41$  MA/m,  $A_{\text{ex}} = 11 \pm 5$  pJ/m,  $k_{u,x} = 22$  kJ/m<sup>3</sup> and  $\alpha = 0.001$ .

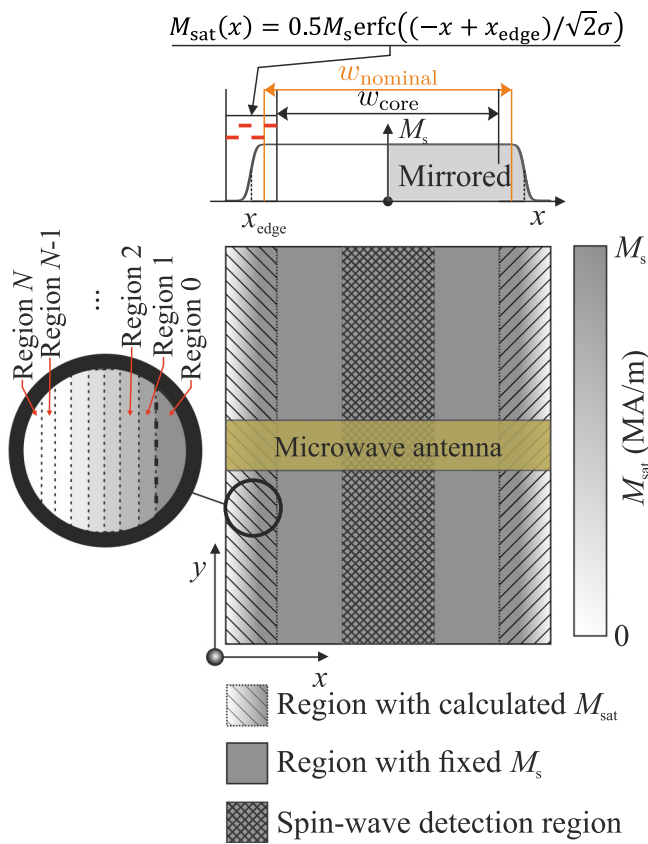


FIG. 5. Schematic definition of the micromagnetic problem. The waveguide is divided into a discrete number of material regions, where the central part is defined as one region. The magnetization in the edge area (schematically magnified in the left part of the image) of the waveguide is modulated by steplike manner where each region has a constant value of  $M_{\text{sat}}(x)$  given by the error function. The excitation antenna is overlaid in the image and has a form of a simple rectangular region. The spin-wave detection region is indicated by a crosshatched area in the center of the core. The spin-wave dispersion is extracted only from this area as in the actual experiment, where we measure only the central part of the waveguide. Above the 2D map, a transverse profile of the magnetization is shown, together with the equation defining  $M_{\text{sat}}(x)$  in the edge region. Individual short red lines in the edge region denote the length of  $2\sigma$ .

The  $k_{ux}$  value differs from the value derived for the anisotropy field  $B_{\text{ani}}$  (24 mT; see above). In the experiment, only the effective value of the anisotropy is measured. The value of  $k_{ux}$  is obtained by summing the experimentally found value of  $k_{u \text{ exp}} = B_{\text{ani}} M_s / 2$  with the estimation of  $k_{u \text{ shape}}$  based on the model by Aharoni [35]. Final tuning of  $k_{ux}$  was performed in the micromagnetic simulations in order to match the frequency of the ferromagnetic resonance (mode with zero  $k$  vector) with the FMR frequency given by the analytical model for  $B_{\text{ani}}$ .

After the initialization of the geometry, the static magnetic field  $B_x$  was applied, and the magnetization was relaxed to the energetical minimum. Subsequently, the field was set to zero, and again the energy minimum was found. Afterwards we excited the waveguide by a localized in-plane magnetic field  $B_y$  with  $\text{sinc}(t)$  time dependence:

$$B_y(t) = B_{\text{max}} \text{sinc}[2\pi f(t - t_0)],$$

where  $B_{\text{max}} = 1$  mT,  $t_0 = 100$  ps, and  $f = 30$  GHz is the cut-off frequency. The dynamic field is localized in a rectangular region spanning over the width of the waveguide ( $x$  direction) and having a length of  $0.5 \mu\text{m}$ . After the excitation, the magnetization vector map in a  $0.5 \mu\text{m}$  wide region is saved every 25 ps for 40 ns. For postprocessing, we load the  $m_z(x, y)$  map and calculate the average value over the width of the central region to obtain  $m_z(y)$  for each time step. This creates a 2D data set  $m_z(y, t)$ . The spatiotemporal matrix is then windowed by the Hann function in order to eliminate windowing artifacts in the subsequent FFT analysis. The dispersion map shown in Fig. 4(b) is then obtained directly by plotting the amplitude of the spatial and temporal frequencies obtained from a two-dimensional fast Fourier transform of  $m_z(y, t)$ :

$$m_z(k_{\parallel}, \omega) = \mathcal{F}[m_z(y, t)].$$

These data still contain some artifacts, e.g., nonuniform excitation in the  $k$  space due to the rectangular antenna shape. Deconvolution of the obtained dispersion with the Fourier image of the antenna shape and the excitation pulse would enhance the data quality even further yet does not reveal any new phenomena in the presented data. For this reason and for the sake of simplicity we did not employ this step in our data processing.

- [1] S. Neusser and D. Grundler, *Adv. Mater.* **21**, 2927 (2009).
- [2] A. V. Chumak, V. I. Vasyuchka, A. A. Serga, and B. Hillebrands, *Nat. Phys.* **11**, 453 (2015).
- [3] E. Albisetti, D. Petti, G. Sala, R. Silvani, S. Tacchi, S. Finizio, S. Wintz, A. Calò, X. Zheng, J. Raabe, E. Riedo, and R. Bertacco, *Commun. Phys.* **1**, 56 (2018).
- [4] K. Wagner, A. Kákay, K. Schultheiss, A. Henschke, T. Sebastian, and H. Schultheiss, *Nat. Nanotechnol.* **11**, 432 (2016).
- [5] M. Vogel, R. Abmann, P. Pirro, A. V. Chumak, B. Hillebrands, and G. von Freymann, *Sci. Rep.* **8**, 11099 (2018).
- [6] A. V. Chumak, A. A. Serga, and B. Hillebrands, *Nat. Comm.* **5**, 4700 (2014).
- [7] W. Rupp, A. Biedermann, B. Kamenik, R. Ritter, Ch. Klein, E. Platzgummer, M. Schmid, and P. Varga, *Appl. Phys. Lett.* **93**, 063102 (2008).
- [8] J. Gloss, S. S. Shah Zaman, J. Jonner, Z. Novotný, M. Schmid, P. Varga, and M. Urbánek, *Appl. Phys. Lett.* **103**, 262405 (2013).
- [9] M. Urbánek, L. Flajšman, V. Křížáková, J. Gloss, M. Horký, M. Schmid, and P. Varga, *APL Mater.* **6**, 060701 (2018).
- [10] C. Chappert, H. Bernas, J. Ferre, V. Kottler, J.-P. Jamet, Y. Chen, E. Cambril, T. Devolder, F. Rousseaux, F. Mathet, and H. Launois, *Science* **280**, 1919 (1998).
- [11] R. Bali, S. Wintz, F. Meutzner, R. Hubner, R. Boucher, A. A. Unal, S. Valencia, A. Neudert, K. Potzger, J. Bauch, F. Kronast,

- S. Facsko, J. Lindner, and J. Fassbender, *Nano Lett.* **14**, 435 (2014).
- [12] F. Roder, G. Hlawacek, S. Wintz, R. Hübner, L. Bischoff, H. Lichte, K. Potzger, J. Lindner, J. Fassbender, and R. Bali, *Sci. Rep.* **5**, 16786 (2015).
- [13] K. Vogt, F. Y. Fradin, J. E. Pearson, T. Sebastian, S. D. Bader, B. Hillebrands, A. Hoffmann, and H. Schultheiss, *Nat. Comm.* **5**, 3727 (2014).
- [14] C. L. Ordóñez-Romero, Z. Lazcano-Ortiz, A. Drozdovskii, B. Kalinikos, M. Aguilar-Huerta, J. L. Domínguez-Juárez, G. López-Maldonado, N. Qureshi, O. Kolokotsev, and G. Monsivais, *J. Appl. Phys.* **120**, 043901 (2014).
- [15] C. Bayer, J. Jorzick, B. Hillebrands, S. O. Demokritov, R. Kouba, R. Bozinoski, A. N. Slavin, K. Y. Guslienko, D. V. Berkov, N. L. Gorn, and M. P. Kostylev, *Phys. Rev. B* **72**, 064427 (2005).
- [16] B. Obry, P. Pirro, T. Brächer, A. V. Chumak, J. Osten, F. Ciubotaru, A. A. Serga, J. Fassbender, and B. Hillebrands, *Appl. Phys. Lett.* **102**, 202403 (2013).
- [17] J. Fassbender, J. von Borany, A. Mücklich, K. Potzger, W. Moller, J. McCord, L. Schultz, and R. Mattheis, *Phys. Rev. B* **73**, 184410 (2006).
- [18] L. Flajšman, M. Urbánek, V. Křižáková, M. Vaňatka, I. Turčan, and T. Šíkola, *Rev. Sci. Instrum.* **87**, 053704 (2016).
- [19] The anisotropy field is called effective as we see only the result of the two competing contributions: crystalline uniaxial magnetic anisotropy coming from the FIB writing process and from the uniaxial shape anisotropy having its origin in the shape of the waveguide (approximately 7 mT for the 1.5  $\mu\text{m}$  wide waveguide). The total anisotropy of the structure is then obtained as the difference of the two contributions.
- [20] T. Sebastian, K. Schultheiss, B. Obry, B. Hillebrands, and H. Schultheiss, *Front. Phys.* **3**, 35 (2015).
- [21] V. E. Demidov, S. O. Demokritov, K. Rott, P. Krzysteczko, and G. Reiss, *Appl. Phys. Lett.* **92**, 232503 (2008).
- [22] J. P. Park, P. Eames, D. M. Engebretson, J. Berezovsky, and P. A. Crowell, *Phys. Rev. Lett.* **89**, 277201 (2002).
- [23] K. Vogt, H. Schultheiss, S. J. Hermsdoerfer, P. Pirro, A. A. Serga, and B. Hillebrands, *Appl. Phys. Lett.* **95**, 182508 (2009).
- [24] B. A. Kalinikos and A. N. Slavin, *J. Phys. C* **19**, 7013 (1986).
- [25] K. Yu. Guslienko, S. O. Demokritov, B. Hillebrands, and A. N. Slavin, *Phys. Rev. B* **66**, 132402 (2002).
- [26] V. E. Demidov, M. P. Kostylev, K. Rott, P. Krzysteczko, G. Reiss, and S. O. Demokritov, *Appl. Phys. Lett.* **95**, 112509 (2009).
- [27] V. E. Demidov, S. O. Demokritov, K. Rott, P. Krzysteczko, and G. Reiss, *Phys. Rev. B* **77**, 064406 (2008).
- [28] O. Gladii, D. Halley, Y. Henry, and M. Bailleul, *Phys. Rev. B* **96**, 174420 (2017).
- [29] J. F. Ziegler, M. D. Ziegler, and J. P. Biersack, *Nucl. Instrum. Methods Phys. Res. B* **268**, 1818 (2010).
- [30] S. S. Zaman, P. Dvořák, R. Ritter, A. Buchsbaum, D. Stickler, H. P. Oepen, M. Schmid, and P. Varga, *J. Appl. Phys.* **110**, 024309 (2011).
- [31] R. D. McMichael and B. B. Maranville, *Phys. Rev. B* **74**, 024424 (2006).
- [32] A. Vansteenkiste, J. Leliaert, M. Dvornik, M. Helsen, F. Garcia-Sanchez, and B. Van Waeyenberge, *AIP Adv.* **4**, 107133 (2014).
- [33] C. Kittel, *Phys. Rev.* **110**, 1295 (1958).
- [34] G. Venkat, D. Kumar, M. Franchin, O. Dmytriiev, M. Mruczkiewicz, H. Fangohr, A. Barman, M. Krawczyk, and A. Prabhakar, *IEEE Trans. Magn.* **49**, 524 (2013).
- [35] A. Aharoni, *J. Appl. Phys.* **83**, 3432 (1998).